

# On the possibility of radar echo detection of ultra-high energy cosmic ray- and neutrino-induced extensive air showers

Peter W. Gorham

*Jet Propulsion Laboratory, Calif. Inst. of Technology  
4800 Oak Grove, Drive, Pasadena, CA, 91109 USA*

## ABSTRACT

We show that cosmic-ray air showers resulting from primary particles with energies above  $10^{18}$  eV should be straightforward to detect with radar ranging techniques, where the radar echoes are produced by scattering from the column of ionized air produced by the shower. If our analysis is correct, such systems could provide highly complementary measurements of air showers detected in existing and planned ground arrays such as the Fly's Eye or the Auger Project, and crucial additional information for proposed space missions such as OWL/AirWatch. The technique is particularly sensitive to showers that are transverse to and relatively distant from the detector, and is thus effective in characterization of penetrating horizontal showers such as those that might be induced by ultra-high energy neutrino primaries.

*Subject headings:* cosmic-rays: cosmic-ray detectors, extensive air showers — neutrinos: neutrino detectors — radar — meteor radar

## 1. Introduction

Extensive air showers (EAS) resulting from primary cosmic-ray particles of energies above 1 EeV ( $10^{18}$  eV) produce an ionization trail which is comparable to that of micro-meteors, which have been detected for many decades using radar methods (Lovell 1948; Greenhow, 1952; Hanbury Brown & Lovell 1962). EAS ionization trails are now commonly detected by their fluorescence emission at visible wavelengths (cf. Baltrusaitas et al. 1985). Future large EAS detector arrays such as the Auger project (Guérard et al. 1998) and the proposed space mission OWL/AirWatch (Scarsi et al. 1999; Krizmanic et al. 1999) have made fluorescence detection of EAS a centerpiece of their approach, since it can provide information such as the position of the shower maximum and the total shower energy which are often difficult to pin down with particle detectors alone. One of the most compelling reasons to extend the sensitivity of EAS detectors in this energy regime is the possibility that neutrinos of energy  $\geq 10^{19}$  eV may be an important component of the primary particles (Capelle et al. 1999). Yet to our knowledge no one has yet attempted to study the ionization trail of these events using radar echo techniques, although as we will show here, the signals should be clearly detectable using standard methods used in studying meteors for decades.

Meteor ionization trails are commonly parameterized in terms of their ionization line density  $\alpha$  (electrons  $\text{m}^{-1}$ ), a measure of the total ionization content divided by the length of the meteor track. Typical radar-detected meteors occur at heights of 80–120 km, and have line densities of  $\alpha = 10^{13}$  to  $10^{16}$   $\text{m}^{-1}$ . At the lowest detectable line densities, the incident meteor has a mass of  $\sim 10^{-10}$  kg, with a radius less than 100  $\mu\text{m}$ . At typical velocities of  $\sim 30$   $\text{km s}^{-1}$ , the implied kinetic energy of these meteor grains is 0.05 Joules or more, much of which goes into ionization of the air along its path.

A cosmic ray proton of energy  $10^{18}$  eV has a kinetic energy also of order 0.1 J, and much of this energy also ultimately ends up in the form of ionization and excitation of atoms of the air along the path of the shower of charged particles that results from the proton’s collision with nuclear hadrons. The primary differences between the meteor track and cosmic-ray-induced EAS are in the way the ionization column forms, and in the resulting ionization density profile.

For the meteor, ablation of material from its surface yields atoms with kinetic energies of  $10^2 - 10^3$  eV, which ionize air molecules by direct collision with a mean free path of several cm. This yields an ionization column with an approximately Gaussian distribution of radial density, and an initial radius of order 1 m or less. The density then evolves with time due to diffusion, convective processes, bulk motions of the air, and the Lorentz forces of the ambient electric and geomagnetic fields. Recombination also eventually plays a role, though not a dominant one. At radar frequencies in the lower VHF range (30–100 MHz), echoes from typical meteors may be detectable for several seconds after the meteor is gone.

The ionization in an EAS, in contrast, is not produced by a single body, but rather by the collective effects of the disk highly energetic particles (mostly electrons and positrons) that make up the body of the shower. Because the lateral distribution of these particles spreads out as the shower progresses, the ionization column is formed with a different initial distribution than that of a meteor, reflecting the evolution of the cross-sectional charged particle density. In addition, since the shower propagates essentially at the speed of light, it appears almost instantaneously compared to even the fastest meteors at  $\sim 100$   $\text{km s}^{-1}$ .

An important measure of the transverse charged particle distribution in an EAS is the Moliere radius  $r_m$  within which of order 90% of the charged particles can be found. For air at sea level,

$r_m \simeq 70\text{m}$ , but it is important to note that within  $r_m$  the radial distribution is a power law, and most showers retain a tight core of particles of diameter several m or less.

In the following section we present the concept of the radar cross section (RCS) and outline specific cases relevant to EAS ionization columns. Section 3 develops a semi-analytical method for determining the ionization densities for a given air shower energy and altitude, and discusses some issues related to recombination of the ions. Section 4 then makes estimates of the radar echo power based on the formalism developed in the previous two sections. Section 5 concludes the paper with a discussion of some applications to specific experimental conditions.

## 2. Radar detection of ionization columns

For radar detection of the columns that result from either meteors or EAS events, there are two regimes to consider, depending on the plasma frequency  $\nu_p$  of the ionized region:

$$\nu_p = \sqrt{(n_e e^2 / \pi m_e)} \simeq 8.98 \times 10^3 \sqrt{n_e} \text{ Hz} \quad (1)$$

where  $n_e$  is the electron density in  $\text{cm}^{-3}$ . These two regimes are known in the meteor radar community as the under- and over-dense regimes, respectively, and traditionally are divided at the line density of  $\alpha \simeq 10^{14} \text{ m}^{-1}$ . For our purposes, we distinguish them only on the basis of the ratio of radar to plasma frequency.

Radar targets are most commonly described in terms of their effective RCS (RCS), a measure of the equivalent physical area of an ideal scattering surface. Here we will develop concepts useful to understanding the RCS characteristic to ionization columns, to prepare for later estimation of the expected radar return power from EAS-induced ionization.

In the following subsections we introduce general formulas for the RCS for both over- and under-dense cases. An additional distinction is

also useful in each case: the long wavelength, or *Rayleigh* regime involves targets with characteristic dimensions smaller than the radar wavelength used; and the short wavelength, or *optical* regime involves cases where the characteristic target size is much larger than the radar wavelength.

### 2.1. Overdense regime

When the electron density  $n_e(r)$  is high enough to produce a surface where the plasma frequency exceeds the frequency of the incident radiation at some critical radius  $r_c$  from the track, the resulting index of refraction becomes imaginary, and total external reflection of the radiation occurs. Under these conditions, the surface at  $r_c$  can be treated to first order as a metal cylinder, and the RCS is accordingly greatly enhanced.

#### 2.1.1. Optical regime

When  $r_c \gg \lambda$ , the reflection from the critical surface becomes almost entirely specular, and for normal incidence we have (Kraus 1988)

$$\sigma_{b,max} = \frac{2\pi r_c L^2}{\lambda} \quad (2)$$

where  $\sigma_{b,max}$  denotes the maximum value of the RCS, and  $L$  is the length of the cylindrical reflecting surface. Radar cross sections for metal cylinders have been studied in detail (cf. Medgyeshi-Mitschang & Putnam 1985) and are complicated functions of angle, with resonances and nulls that depend strongly on the length and other factors. As we shall establish below, EAS ionization columns will generally not fall into the optical regime for the overdense case, except at very high EAS energies and very low radar frequencies. For this reason we do not treat these effects further here.

#### 2.1.2. Rayleigh regime

When  $r_c \ll \lambda$ , the cylindrical region of the previous section can be approximated as a thin wire. As we will show below, this is the case most

relevant to radar echoes from EAS. In this case the maximum the RCS, which occurs for normal incidence, can be approximated as (Crispin & Maffett 1965):

$$\sigma_{b,max}^{od} \simeq \frac{\pi L^2 \cos^4 \phi}{\left(\frac{\pi}{2}\right)^2 + (\ln[\lambda/(1.78\pi r_c)])^2} \quad (3)$$

where  $\phi$  the angle of polarization with respect to the axis of the wire. The behavior of  $\sigma_b$  at angles other than normal incidence is given by:

$$\sigma_b^{od}(\theta) \simeq \frac{\lambda^2 \tan^2 \theta \cos^4 \phi}{16\pi \left[ \left(\frac{\pi}{2}\right)^2 + (\ln[\lambda/(1.78\pi r_c \sin \theta)])^2 \right]} \quad (4)$$

where  $\theta$  is the angle as measured from the axis of the wire (or EAS in our case). This approximation is valid in the range  $60^\circ \leq \theta \leq 120^\circ$ , but underestimates the cross section at angles closer to the axis of the wire, due to what are known as *traveling wave* effects, which produce large cross sections near the axis, in some cases comparable to that at normal incidence (Medgyeshi-Mitschang & Putnam 1985), and significantly broader in angular range. However, the treatment of such effects is very complex and beyond our scope at present.

In practice the presence of the radial halo of plasma outside of  $r_c$  modifies the dielectric constant and the cylinder at  $r_c$  is partially defocused by the refractive effects. This tends to reduce the RCS by a factor of  $\sim 2$  under typical conditions (Poulter & Baggaley 1977).

## 2.2. Underdense regime

For radar frequencies well above the plasma frequency  $\nu_p$ , the radiation penetrates the entire ionization column, and the electrons within the ionization column scatter independently according to the Thomson cross section  $\sigma_T = (8\pi/3)(e^2/m_e c^2)^2 = 6.65 \times 10^{-29} \text{ m}^2$ . The total effective radar backscatter cross section  $\sigma_b$  will then depend on the individual phase factors of each of the scattering electrons.

### 2.2.1. Rayleigh regime

For  $r_m \ll \lambda$ , and angles that are nearly perpendicular to the track, the electrons scatter coherently over a longitudinal region of the track  $L_F = \sqrt{\lambda R/2}$  where  $R$  is the perpendicular distance to the track and  $\lambda$  the radar wavelength (Hanburay-Brown & Lovell 1962). This region of the track is known as the first Fresnel zone of the track, and the total radar backscatter cross section then becomes

$$\sigma_b = N_e^2 \sigma_T, \quad (5)$$

where  $N_e = \alpha L_F = \alpha \sqrt{\lambda R/2}$  is the number of electrons within a single Fresnel zone along the track. The radar cross section depends of the square of the electron density because of the assumption of full coherence.

Except for radar frequencies  $f \ll 10 \text{ MHz}$ , most radar ranging of EAS ionization columns is not in the Rayleigh regime. However, the concept of the Fresnel zone, which establishes a characteristic length scale over the longitudinal extent of the track, will still be useful in what follows.

### 2.2.2. Optical regime

For tracks where the radar frequency  $f > \nu_p$ , but  $r_m \geq \lambda/4$ , the assumption of coherent scattering is no longer satisfied, and the individual phase factors of the electrons must be included. For this case the effective RCS can be written (cf. Wehner 1987; also see appendix):

$$\sigma_b^{ud}(\mathbf{k}) = \left| \int n_e(\mathbf{r}) \sqrt{\sigma_T} e^{2i\mathbf{k} \cdot \mathbf{r}} d^3\mathbf{r} \right|^2 \quad (6)$$

where  $\mathbf{k}$  is the wave vector of the incident field ( $k = 2\pi/\lambda$ ),  $\mathbf{r}$  is the vector distance to the volume element at which the scattering takes place. Here we are neglecting refractive effects of the ionization column on the incident radiation, and assuming that the incident and reflected waves satisfy  $\mathbf{k} \parallel \mathbf{r}$ .

Note that the argument of the exponential here includes an extra factor of two to represent

the two-way phase. This is due to the fact that as the scattered radiation returns on the same path as the incident radiation, it picks up an additional phase factor equal to that of the incoming radiation. The term  $n_e(\mathbf{r})\sqrt{\sigma_T}$  represents the differential contribution to the scattered electric field of a volume element of electrons which scatter coherently.

If we now write  $\mathbf{q} = 2\mathbf{k}$  then equation 6 becomes

$$\sigma_b^{ud}(\mathbf{q}) = \sigma_T \left| \int n_e(\mathbf{r}) e^{i\mathbf{q}\cdot\mathbf{r}} d^3\mathbf{r} \right|^2 \quad (7)$$

Equation 7 thus reduces the problem of estimating the effective cross section in the underdense case to that of calculating the Fourier transform (and the resulting power spectrum) of the electron number density distribution. In the appendix we describe the geometry more explicitly and show how this relation arises.

A broader implication of this result is that a measurement of the complex amplitude of the radar echo in the underdense case is equivalent to a measurement of one Fourier component of the shower ionization profile.

### 3. EAS ionization densities

In the previous section we introduced the mechanisms for radar reflection from cylindrical plasma columns in two regimes of ionization density. Here we estimate the expected ionization from a high energy cosmic-ray air shower.

#### 3.1. Longitudinal ionization

There are many years of development of the theory of EAS production. The most accurate treatments of the evolution of the electron density in the shower require numerical simulations, but there are a number of parameterizations available that yield results accurate enough for our needs. Here we use the analytical model due originally to Kamata & Nishimura (1958),

and Greisen (1965). In this model the longitudinal (along-track) development of the shower at a depth  $d$  is parameterized by its *age*  $s$ :

$$s(d) = \frac{3d/X_0}{d/X_0 + 2\ln(E/E_{crit})} \quad (8)$$

where  $E_{crit} = 86$  MeV for electrons in air, and  $X_0 = 36.7$  gm cm<sup>-2</sup> is the electron radiation length in air. The evolution of the total number of charged particles (virtually all electrons & positrons) with depth is then approximated by

$$N_e = \frac{0.31 \exp[(d/X_0)(1 - 1.5 \ln s)]}{\sqrt{\ln(E/E_{crit})}}. \quad (9)$$

Although this approach does not account for any of the large fluctuations that are possible in high energy air showers, it describes the average behavior reasonably well.

#### 3.2. Transverse ionization density

The transverse charged particle densities are described in a similar fashion, also parameterized by the age of the shower and the Moliere radius  $r_m$  (Bourdeau 1980):

$$\xi_e = K_N \left( \frac{r}{r_m s_m} \right)^{s-2} \left( 1 + \frac{r}{r_m s_m} \right)^{s-4.5} \quad (10)$$

where

$$K_N = \frac{N_e}{2\pi r_m^2 s_m^2} \frac{\Gamma(4.5 - s)}{\Gamma(s)\Gamma(4.5 - 2s)} \quad (11)$$

and  $\Gamma$  is the gamma function, and  $s_m = 0.78 - 0.21s$ . The Moliere radius can be approximated as  $r_m = 2.12 \times 10^7 X_0 (E_{crit} \rho_{air})^{-1}$  cm. The calculated density  $\xi_e$  is in units of charged particles per unit area, passing through a plane transverse to the shower axis at the given depth. Since the shower thickness is typically of order several meters or less over its length,  $\xi_e$  can be approximately equated with the number density in a slab transverse to the shower.

To convert these particle number densities to the resulting ionization density, we use the average value for electron energy loss given by

$E_{crit}/X_0 = 2.343 \text{ MeV gm}^{-1} \text{ cm}^{-2}$ , divided by the mean energy per ion-pair for air  $E_{ion} = 33.8 \text{ eV}$  (Segre 1977) which accounts for the inefficiency of ion-pair production. This procedure is similar to that used by the Fly's Eye (Baltrušaitis et al. 1985) in estimating shower parameters based on fluorescence yield.

### 3.3. Numerical results

Fig. 1 shows curves of calculated ionization line densities for several EAS of different primary energies over the range of  $10^{18} - 10^{21} \text{ eV}$ . The showers are assumed to be propagating horizontally at an altitude of 10km, and the shower parameters are corrected for the lower air density at this altitude. The bottom axis shows the along-track distance corresponding to the depth shown along the top axis. As noted above, the line densities at these energies correspond to typical line densities of radio meteors, which are detected at heights of 80-120 km. We note that the showers are physically very long, with the region of shower maximum extending over many km of physical distance for most showers at these energies.

In Fig. 2, we show the lateral ionization density distributions near shower maximum for the same 5 EAS presented in Fig. 1 (solid lines). Included also are curves of the effective plasma frequency corresponding to the density at each radial distance (dashed lines). Given the uncertainty in the accuracy of the analytical model for EAS development at very small core radii (cf.  $r < 20 \text{ cm}$ ), the implied highest radar frequencies that will undergo total reflection are in the range of 10-50 MHz, with a strong dependence on the primary energy.

### 3.4. Diffusion of the column & the echo decay time

Before estimating the radar echo power, we digress briefly on the important topic of the expected duration of the echo. For EAS detection

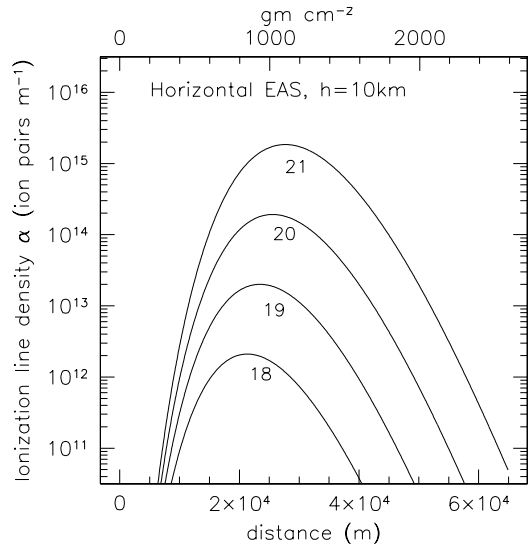


Fig. 1.— Electron ionization line density for 5 showers of energies in the  $10^{18}$  to  $10^{21} \text{ eV}$  range. Such line densities are quite similar to those of radio meteors.

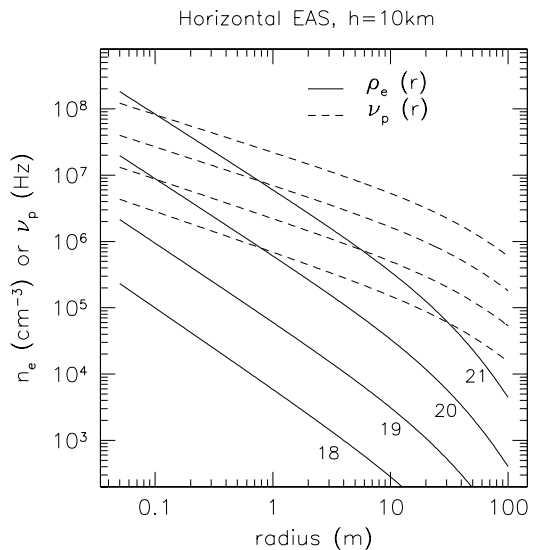


Fig. 2.— Radial dependence of the ionization density for the same showers presented in the previous figure. Also shown is the radial dependence of the plasma frequency for each case.

it is necessary to first establish that the ionization column can be treated as quasi-static over the timescale it might take to interrogate the shower with a radar system, for example, if a separate air shower detector provided the trigger. For typical electronics used in such systems the trigger forms within  $10^{-8}$  s or so, and we may reasonably expect that the radar pulse could be triggered within several microseconds. Transit time to an EAS within  $\sim 30$  km requires another  $100\mu\text{s}$ . Thus we require EAS ionization to retain quasi-static behavior for of order 1 ms or longer. This means that effects such as diffusion and recombination of the electrons must have characteristic times that are long compared to  $\sim 1$  ms.

The duration of meteor radar echoes has been modelled and studied in detail for many decades (cf. Hanbury Brown & Lovell 1957; Kaiser 1968; Kaiser et al. 1969; Jones & Jones 1990; Jones 1991). The power of a meteor radar echo is found in the underdense regime to decay exponentially with a time constant  $\tau_m = \lambda^2 / (32\pi^2 D_i)$  where  $D_i$  is the ambipolar (or ion neutral) diffusion coefficient. At the altitudes that meteors are observed with radar,  $D_i \simeq 1 - 10 \text{ m}^2 \text{ s}^{-1}$ , and the typical decay times for underdense trails are thus several tens of ms for frequencies in the VHF regime.

To estimate diffusion effects at the lower altitudes of EAS ionization columns, we note that  $D_i \propto T\nu_i^{-1}$  where  $T$  is the kinetic temperature and  $\nu_i$  the collision frequency (cf. Buonsanto et al. 1997). Thus at 10 km altitude, the diffusion coefficient is much smaller,  $D_i \sim 5 \text{ cm}^2 \text{ s}^{-1}$ , due mainly to the much higher collision frequency at lower altitudes. The implied time constant, assuming diffusion progresses in the same manner for EAS as for meteor ionization columns, is  $\tau_{eas} \simeq 60 \text{ s}$  for  $\lambda = 3 \text{ m}$ .

Since diffusion is less effective at dissipating the ionization column of an EAS than it is for a meteor, we might expect that recombination may play a more significant role, since the electron number density will remain high for a longer period than for meteor ionization. The recombi-

nation rate for atmospheric electrons is described by (Thomas 1971):

$$\frac{dn_e}{dt} = -\alpha_i n_e^2 \quad (12)$$

where  $\alpha_i$  is the electron-ion recombination coefficient (in units of  $\text{cm}^3 \text{ s}^{-1}$ ) and  $n_e$  is the electron density. Here we have ignored terms in Thomas (1971) which relate to the presence of negative ions in the ionosphere since we are considering EAS within the troposphere where such ions are not prevalent. The total recombination coefficient for hydrogenic atoms can be approximated by (Seaton 1959)

$$\alpha_i = 5.20 \times 10^{-14} Q^{1/2} \times (0.429 + 0.5 \ln Q + 0.469 Q^{-1/3}) \text{ cm}^3 \text{ s}^{-1}$$

where  $Q = 1.58 \times 10^5 / T_e$  and  $T_e$  is the electron kinetic temperature, with  $T_e \simeq 10^3 - 10^4 \text{ K}$  typical for ionization in this case. For air in the troposphere we thus expect  $\alpha_i \sim 10^{-12}$  to  $10^{-11} \text{ cm}^3 \text{ s}^{-1}$ , and the implied recombination time for the highest electron densities we have considered is several minutes or more.

We note that values of  $\alpha_i = 2 \times 10^{-7} \text{ cm}^3 \text{ s}^{-1}$  are found in the D region of the ionosphere (Thomas 1971). Such a high value is likely to be due to the large variety of ion species present, which increases the total recombination cross section per electron. In fact the recombination coefficient appropriate for meteor trails is expected to be closer to  $10^{-12} \text{ cm}^3 \text{ s}^{-1}$  (Hanbury Brown & Lovell 1962). However, since we know of no direct measurements of tropospheric values for  $\alpha_i$ , we consider the impact of a recombination coefficient of this magnitude on EAS ionization.

If we numerically integrate equation 12 above using the largest values of  $\alpha_i$  seen in the ionosphere as noted above, and the highest ionization line densities (thus the highest EAS energies) we can derive an estimate of the shortest likely recombination time associated with EAS ionization columns. Fig. 3 shows the results of this for the

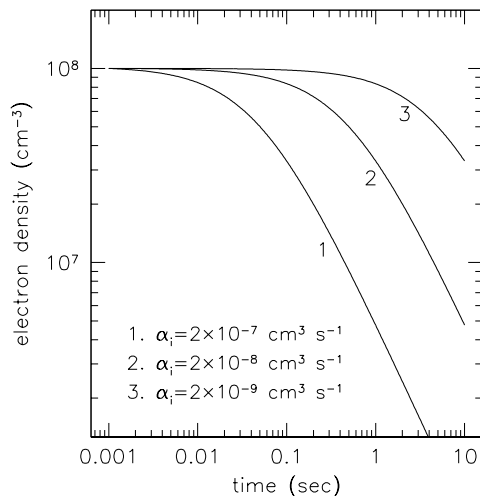


Fig. 3.— Recombination profile of core electron density for a shower of  $E_0 = 10^{21}$  eV and three values of the recombination coefficient  $\alpha_i$ . The maximum value of  $\alpha_i$  represents the highest estimated daytime value for the D region of the ionosphere (Thomas 1971), and thus provides a conservative estimate of the shortest possible recombination time in the troposphere. Recombination times are much longer for lower energy showers.

value above, and two other lower of  $\alpha_i$  that begin to approach our expected values. The plot shows the time evolution of the electron number density for a starting value roughly equal to the highest density value in the core of a shower with  $E_0 = 10^{21}$  eV. In the worst case the core density decays to half its initial value over a period of 40 ms, which still provides adequate time to interrogate the shower many times with a radar pulse.

It thus appears unlikely that either diffusion or recombination are significant in reducing the ionization from EAS over the  $\sim 1$  ms time scale necessary to interrogate it with a radar pulse. Instead, we expect that other effects, such as bulk convection or wind turbulence, will act to dissipate the ionization over time scales of order several seconds or more.

#### 4. Predicted radar return power from EAS

Having established the plausibility of detecting EAS radar echoes, and introduced the RCSs expected, we now turn to estimation of the return power of the echo.

Radar return power  $P_r$  is described in terms of a model where the radiation is emitted from an antenna with peak transmitted power  $P_t$  and directivity gain  $G = 4\pi\Omega_A^{-1}$ , where  $\Omega_A$  is the solid angle of the main beam of the antenna. The radiation is assumed to then scatter from objects in the antenna beam and be re-radiated isotropically in the frame of the scatterer, producing a  $R^{-4}$  dependence in the returned power as a function of range  $R$ . Deviations from isotropic scattering are thus absorbed into the effective radar backscatter cross-section  $\sigma_b$ , which can be larger or smaller than the physical cross-section of the object. In addition any real transmitting and receiving system will have less than unity efficiency, which we designate here as  $\eta$ . The radar equation under these conditions is (cf. Skolnik 1990)

$$\frac{P_r}{P_t} = \sigma_b \eta \frac{G^2 \lambda^2}{(4\pi)^3 R^4}. \quad (13)$$

Here we are assuming that the transmitting and



receiving antennas are identical, and we are neglecting for the moment any polarization effects or losses in the medium.<sup>1</sup>

Given equation 13, the problem of determining the detectability of EAS-initiated ionization columns reduces to that of determining the effective RCS  $\sigma_b$  for a given choice of operating radar frequency, and the noise power of the specific radar in use. The noise power is given by  $P_N = kT_{sys}\Delta f$ , where  $T_{sys}$  is the system noise temperature,  $k$  is Boltzmann's constant, and  $\Delta f$  the effective receiving bandwidth, assumed here to be matched to the transmitting bandwidth.

**Pulse compression.** Almost all modern radar systems now use what is known as *pulse compression*, a method which allows the receiver bandwidth, and thus the noise power, to be minimized (cf. Wehner 1987). Pulse compression is typically implemented by effectively dispersing a band-limited pulse with an initial bandwidth  $\Delta f_0 = (\Delta t_0)^{-1}$  through a filter, transforming it into a frequency chirp which spans the original bandwidth, but now has a duration  $\Delta t \gg \Delta t_0$ . The receiver then uses an inverse filter to de-disperse the received pulse. The effective bandwidth is thus  $\Delta f = (\Delta t)^{-1}$ , but the range resolution  $\Delta R \propto \Delta t_0$  of the full bandwidth is recovered.

Combining the noise power equation above with equation 13, the signal-to-noise ratio (SNR) of the received power is

$$\frac{P_r}{P_N} = \sigma_b P_t \eta \frac{G^2 \lambda^2}{(4\pi)^3 R^4} \frac{1}{kT_{sys}\Delta f}. \quad (14)$$

Evaluating equation 14 for a nominal choice

<sup>1</sup>This equation is also derived strictly under conditions where the received radiation is in the far-field, that is, where  $R > 2D^2/\lambda$  where  $D$  is the largest projected dimension of the scattering target. In our case, this is not generally satisfied, since the length of the ionization columns can be tens of km. However, we have already accounted for these Fresnel zone effects by limiting our analysis to the first Fresnel zone as noted above.

of parameters gives the SNR per received radar pulse per square meter of RCS:

$$\begin{aligned} \frac{S}{N} = & 3.3 \left( \frac{\sigma_b}{1 \text{ m}^2} \right) \left( \frac{P_t}{1 \text{ kW}} \right) \left( \frac{\eta}{0.1} \right) \left( \frac{G}{10} \right)^2 \\ & \times \left( \frac{\lambda}{3 \text{ m}} \right)^2 \left( \frac{R}{10^4 \text{ m}} \right)^{-4} \left( \frac{T_{sys}}{10^3 \text{ K}} \right)^{-1} \left( \frac{\Delta t}{10 \text{ } \mu\text{s}} \right). \end{aligned} \quad (15)$$

We note that the reference values chosen here represent a modest radar system; in particular the peak power of 1 kW is easily attained by current standards, and the directivity  $G \simeq 10$  (beam size  $\sim 1$  sr) represents a relatively low-gain antenna. The system temperature  $T_{sys} = 1000$  K is realistic for 100 MHz ( $\lambda = 3$  m) however, since the brightness temperature of the sky is quite high at these frequencies.

Radar systems also routinely use repetitive pulsing to increase SNR, which then grows roughly as  $N_p^{1/2}$  where  $N_p$  is the number of pulses that are averaged. In the case of an EAS, the number of repetitions is limited by the diffusion time of the ionization column. Based on the behavior of meteor trails and the analysis presented above, this time could be several seconds, and the shower ionization density is likely to be almost unchanged over perhaps hundreds of ms, allowing for  $N_p \sim 100$  or more.

We now consider in detail the expected RCS for EAS ionization columns in the various density regimes that were introduced above.

#### 4.1. Low-frequency/overdense case

At radar frequencies below the plasma frequency of the ionized core of the EAS, the RCS is comparable to that of a metal cylinder, as noted above, with a radius of  $r_c$  and a length equal to that of the Fresnel zone. Based on the analytical shower model used above and the results in Fig. 2, the critical radius at a given wavelength and EAS cascade energy  $E_0$  can be empirically

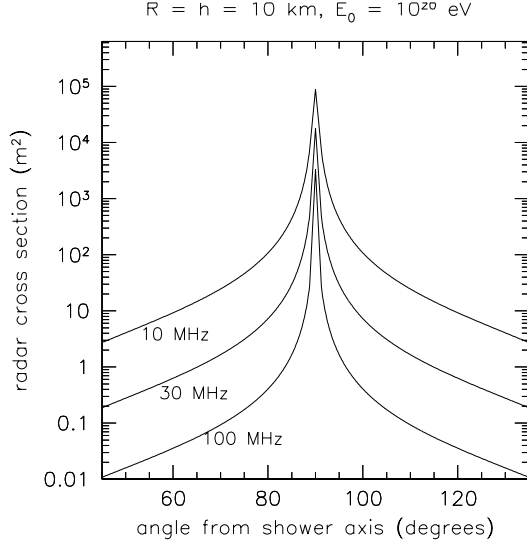


Fig. 4.— Radar cross section over a range of angles centered on normal incidence (at  $90^\circ$ ) for an air shower with  $E_0 = 10^{20}$  eV, at a distance of 10 km, at radar wavelengths 30, 10, and 3 m. Results are based on the thin wire approximation. The polarization of the incident wave has been taken to be aligned with the shower axis.

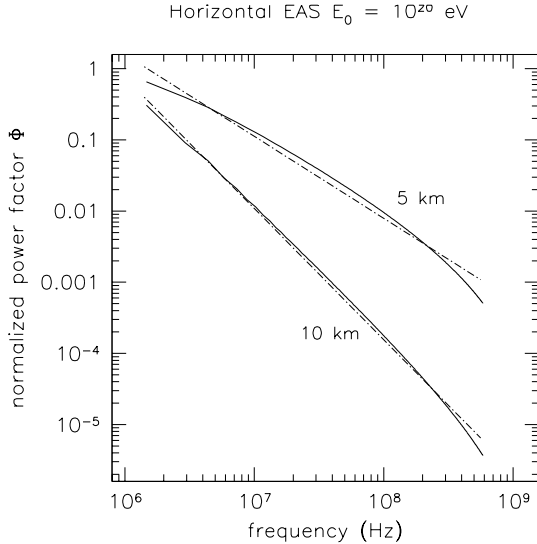


Fig. 5.— Normalized power loss factor due to loss of coherence for two horizontal  $E = 10^{20}$  eV showers at heights of 5 and 10 km.

approximated by

$$\frac{r_c}{\lambda} = \frac{1}{30} \left( \frac{f}{10 \text{ MHz}} \right)^{-0.75} \left( \frac{E}{10^{20} \text{ eV}} \right)^{0.85} \text{ m.} \quad (16)$$

It is evident from this result that for frequencies above 10 MHz, and for all but the highest EAS energies considered here,  $r_c \ll \lambda$  and we can use the thin wire approximation discussed above.

In Fig. 4 we show results for radar cross sections of the first Fresnel zone for a shower of  $E_0 = 10^{20}$  eV, for three different frequencies, for a range of angles centered on normal incidence. The cross section at normal incidence is greatly enhanced due to the specular reflection at that angle. We can empirically express the maximum cross section for this case as <sup>2</sup>

$$\sigma_b^{od}(10 \text{ km}) = 2.6 \times 10^4 \left( \frac{f}{30 \text{ MHz}} \right)^{-1.45} \times \left( \frac{E}{10^{20} \text{ eV}} \right)^{0.44} \left( \frac{R}{10 \text{ km}} \right) \text{ m.} \quad (17)$$

Using this cross section in equation 1 above, we see that such events should be easily detectable with a modest radar system over a range of angles of order  $\pm 10^\circ$  from normal incidence, out to distances of several tens of km. For example, from Fig. 4 we note that at 30 MHz ( $\lambda = 10$  m), (where the sky brightness temperature is  $\sim 12000$  K),  $\sigma_b \geq 5 \text{ m}^2$  over  $\pm 10^\circ$  of normal incidence, for an EAS with  $E_c = 10^{20}$  eV. This gives a  $\text{SNR} \geq 16$  per  $10 \mu\text{s}$  pulse at  $P_t = 1 \text{ kW}$  and a shower range of 10 km.

Here we have ignored the additional contribution due to the partially coherent scattering of the much larger volume of underdense plasma outside of  $r_c$ ; this additional scattering will act to

<sup>2</sup>Here the linear increase of the cross-section with shower impact parameter  $R$  is due to the fact that the size of the first Fresnel zone grows with distance. In fact, although we have used the length of the Fresnel zone  $L_F$  as the characteristic length of the “thin wire” portion of the shower, the actual length of this region is likely to be much longer than  $L_F$ .

increase the cross section particularly at angles away from normal incidence as we will show in the following section. In addition, the traveling wave effects noted previously become important for angles beyond  $\sim 30^\circ$  from normal incidence and these will also act to increase the cross section at larger angles.

Clearly a fully optimized system would not be limited to merely detecting and ranging such events but could also characterize the ionization profile in detail. However, the rapid increase in sky brightness temperature below 30 MHz (Kraus 1988) makes it difficult to take advantage of the large cross sections in the overdense case for showers below  $\sim 10^{20}$  eV.

## 4.2. High-frequency/underdense case

When either the frequency is high enough or the ionization density low enough that there is effectively no region of the column where the critical density obtains, the radar return is due to Thomson scattering of the free electrons in the column, modulated by the phase factor associated with the physical extent of the ionized region as described in equation 7 above.

We have made numerical estimates of the effective cross section for a restricted set of cases here, with the methods described in more detail in an appendix. Here we summarize the results.

### 4.2.1. Normal incidence

For the case of radar observations at normal incidence to the shower, the near constancy of the ionization density along the track allows us to estimate the frequency dependence of the phase factor via a Fast Fourier transform (FFT) of the two dimensional ionization distribution in a plane transverse to the track. We have taken advantage of this feature to make numerical estimates of the frequency-dependent behavior of the phase factors at normal incidence.

Note that the requirement of normal incidence for the radar rays interrogating the shower is not

as restrictive as it might seem. For example, a horizontal shower whose maximum is at a range of  $R_1$  from the radar transmitter/receiver system, and whose axis is inclined an angle  $\theta$  with respect to the ray that joins the radar source and the shower maximum, will still have a ray that intersects the shower at normal incidence at a distance  $R_1 \cos \theta$  from the shower maximum.

For example, a horizontal shower at 10 km altitude, with 15 km range to its maximum, and inclined at  $\theta = 60^\circ$  will have a ray that intersects it at normal incidence at a longitudinal distance along the shower of 7.5 km from shower maximum, at a range of 13 km, where the ionization line density is still  $\sim 60\%$  of its maximum value. Thus the corresponding acceptance solid angle over which these results apply is not negligible.

Fig. 5 shows our estimates of the frequency dependence of the phase factor for two horizontal showers at altitudes of 5 and 10 km, for  $E_0 = 10^{20}$  eV. The phase factor depends strongly on both frequency and shower altitude. The frequency dependence is due to loss of coherence as noted above, and the altitude dependence arises from the change in Moliere radius to smaller values at lower altitudes. We have also investigated the behavior at other energies in this regime and found these results to be insensitive to energy over the range  $10^{18} - 10^{21}$  eV. For the two cases shown we have included fitted power laws

$$\Phi(f; 5 \text{ km}) = 0.114 f_{10}^{-1.15}$$

$$\Phi(f; 10 \text{ km}) = 1.13 \times 10^{-2} f_{10}^{-1.84}.$$

These relations are individually accurate to about 20% over the range from 10 MHz to 0.3 GHz.

Given the power loss associated with the phase factor, the total cross section is then estimated by summing the cross sections of the individual volume elements over one Fresnel zone of the track, by analogy to the overdense case, and multiplying by the overall phase factor for the radar frequency and shower altitude.

Evaluating this modified cross section for its energy and frequency dependence, we derive an

empirical expression for the case of a horizontal EAS at altitude of 10 km

$$\sigma_b^{ud}(10 \text{ km}) = 175 \left( \frac{f}{30 \text{ MHz}} \right)^{-1.84} \times \left( \frac{E}{10^{20} \text{ eV}} \right)^{1.9} \left( \frac{R}{10 \text{ km}} \right) \text{ m.} \quad (18)$$

and similarly for an altitude of 5 km:

$$\sigma_b^{ud}(5 \text{ km}) = 1400 \left( \frac{f}{30 \text{ MHz}} \right)^{-1.15} \times \left( \frac{E}{10^{20} \text{ eV}} \right)^{1.9} \left( \frac{R}{10 \text{ km}} \right) \text{ m.} \quad (19)$$

These relations should be valid out to ranges of several tens of km. At the highest energies and lowest frequencies the underdense case may not obtain, but these estimates will then provide a lower limit on the RCS.

We can use these results to estimate the threshold energy of this technique for ranges of interest to ground EAS arrays such as the Fly's Eye in Utah. At a typical detection range of 5 km, and a similar value for the shower altitude, a horizontal shower of  $10^{18}$  eV has a RCS of  $\sim 1 \text{ m}^2$  at 30 MHz. Using equation 1 above, this cross section produces a SNR of almost 600 for the parameters used, and implies that, at this frequency, showers of  $10^{18}$  eV could be detected out to ranges of order 30 km or more.

#### 4.2.2. Oblique angles

For shower angles away from normal incidence, it is necessary to consider all of the individual scattering contributions of the electrons over the entire volume of the shower, and to treat the pulse echo behavior explicitly. We discuss this in detail in the appendix. We have numerically estimated the integrated RCS for several wavelengths at a distance of 10 km to display some of the characteristics of the angular dependence.

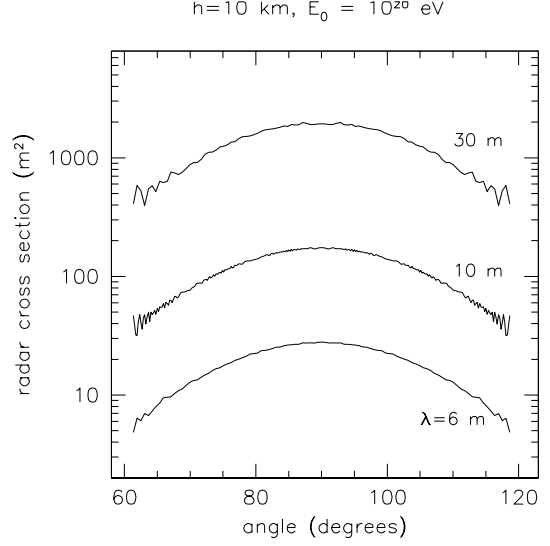


Fig. 6.— Radar cross section over a range of angles centered on normal incidence (at  $90^\circ$ ) for a horizontal air shower with  $E_0 = 10^{20}$  eV, at an altitude of 10 km, at radar wavelengths 30, 10, and 6 m. Results are based on numerically integrating the contributions of all of the individual volume elements of the shower.

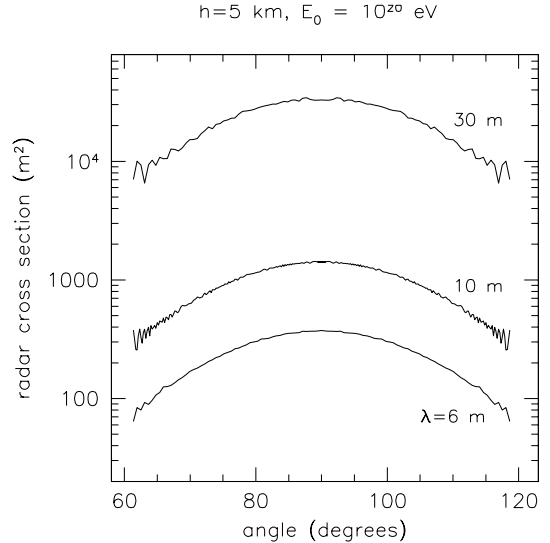


Fig. 7.— Similar to previous figure, with shower altitude of 5 km.

The results of this are shown in Figures 6 and 7. We have plotted the total RCS as a function of angle over about 1 radian around normal incidence, for a horizontal shower at heights 10 and 5 km and energy  $10^{20}$  eV, and several different radar wavelengths. The dependence on angle is quite different from the overdense case where specular reflection is important; here, the cross section has an approximately Gaussian profile with angle, with a FWHM of order  $30^\circ$ . The fairly steep wavelength dependence is also independent of angle over this range. Thus the empirical relations derived in the previous section can be used with appropriate factors for the angle of incidence shown here.

We caution here that the angular dependence of the RCS at distances that are much greater than the length of the shower is probably not accurately reflected by these results. We have not yet derived a general analytical treatment of the behavior for large distances, but we note that the methods described in the appendix allow for numerical estimates to be made at any distance.

### 4.3. Caveats

We note that, due to self-imposed limitations of scope, a number of effects have not been treated in our analysis. We list several of these here.

**Geomagnetic effects.** We have neglected geomagnetic charge separation in the shower development. Although this is an important effect in determining the detailed shower structure, it depends greatly on the shower direction with respect to the magnetic field. Its effect on the RCS would also depend on the angle of observation and the treatment of this complex interaction is beyond our scope at present.

**Landau-Pomeranchuk-Migdal (LPM) effect.** We have neglected the LPM effect in the showers considered here. This effect, which retards the

initial growth of the shower, is important at the energies discussed and should be accounted for in a more detailed treatment. However, it affects primarily shower which interact initially through the electromagnetic rather than the hadronic channel, and thus there are still many EAS at these energies for which the approximation used is still accurate.

**Secondary Fresnel zone echoes.** For simplicity we have only treated the echo from the primary Fresnel zone here. In fact, for the high SNR case, many distinct echoes may be detected from successive Fresnel zones, and these will certainly add significantly to the understanding of any detected shower. On the other hand, for underdense showers that are not observed near normal incidence, the time spread of the return will also tend to decrease the instantaneous SNR. Such effects are important in understanding the response of a radar system to the wide variety of possible EAS directions and relative angles and will need to be explored further in any real application.

**Near vertical EAS.** For convenience we have analyzed a horizontal air shower, but such showers are of general interest, since such highly-inclined showers imply very deep initial interactions and are thus a possible signature of neutrino primaries. For more typical showers with small zenith angles, the Moliere radius changes significantly during the shower development and complicated the analysis considerably. Generalization of our analysis to EAS at all angles is best done with a full numerical simulation.

**Pulse smearing by the shower.** Note that our results for the underdense case above apply in a general way only to non-pulsed radar, since the superposition implied by the Fourier transforms assumes that each Fourier component extends spatially out to dimensions that are much larger

than the shower column. For pulses whose compressed time scale is physically shorter than the time-projected thickness of the ionization column of a shower, we must explicitly account for the behavior of the individual pulse echoes from different portions of the shower. However, the effective RCS corresponding to the integrated power of the echo is still described by our analysis to first order.

A general consideration of the complications arising from the pulsed nature of the radar are beyond our scope at present but must be included in any detailed estimate of the pulsed radar echo behavior. In the appendix we describe a method developed to deal with pulsed-radar reflections, and we utilize this method in some later results.

**Plasma resonance effects.** We have treated the underdense case in a simplified way which neglects the possibility of plasma resonance effects. Such effects are in fact seen in meteor echoes (Poulter & Baggaley 1977) and can play an important role in enhancing the RCS, and in producing more complex time structure in the radar return.

## 5. Discussion

In the previous sections we have presented evidence that EAS ionization columns are well within the range of VHF radar detection for cascade energies above  $\sim 10^{18}$  eV. Now we turn to a discussion of the applicability of this approach to present efforts at detection and characterization of such EAS.

### 5.1. Ground-based radar detection as part of a EAS detector array

The use of radar in conjunction with standard fluorescence detectors as a trigger could prove to be a powerful addition to these systems. For example, as noted above most of the events that triggered the first Fly’s Eye detector in Utah were within a range of  $R = 5$  km (Baltrusaitas et al.

1985). At this range, all of the highest energy events would produce strong radar returns with almost any system. At high signal-to-noise ratios, the timing of the return can be estimated to a precision of order  $\Delta t \simeq [SNR \times \Delta f_0]^{-1}$ , and thus even modest systems could produce several meter precision on the shower impact parameter.

In practice, such a system would probably be best implemented using a phased-array, which could interrogate the approximate direction of the shower within several ms of the trigger formation. This is necessary to avoid loss of coherence due to dissipation of the ionization column. An alternate approach could use a high repetition rate pulsed system with a broad beam, such as a dipole pattern, and the fluorescence detector trigger could then be used to save the appropriate range bins.

Although low frequencies ( $f \leq 30$  MHz) are desirable from the point of view of RCS, the sky temperature at these frequencies increases dramatically and would dilute most of the gain acquired in this manner. In addition interference problems will increase at low frequencies as well. It appears that the optimal frequency range is 30 – 100 MHz, as is the case for meteor observations.

#### 5.1.1. A test case: The Auger observatory

Let us consider what is required for a radar system to enhance the planned Auger air shower array. For convenience we consider a case where each of the Auger fluorescence detectors triggers an associated radar system. The planned fluorescence detectors are required to trigger out to  $\sim 20$  km range (Dawson et al. 1997). At a frequency of 50 MHz ( $\lambda = 6$  m), assuming a radar half-power beamwidth of order 5 km at 20 km (to allow for multiple Fresnel zones), we propose a moderately sparse phased-array with a diameter of order 30 m ( $\sim 40$  antennas) to interrogate the lower altitudes at 20 km distance. The implied average array gain is of order 50 for a set of half-wave dipoles (cf. Balanis 1997) with a steer-

able range down to elevations of  $\sim 15^\circ$ . We note that there are already plans to include antennas and receivers usable in the 30-100 MHz range in the Auger array, to be used for passive detection of radio pulses associated with air showers (Rosner & Wilkerson 1997). Such a system could be easily adapted to receive radar echoes in bistatic mode with the addition of front-end filters designed for the compressed pulses of a small number of radar transmitters. Use of many receiving stations in this manner would yield many Fourier components of EAS so detected, possibly enabling detailed reconstructions of the ionization profile.

The required energy threshold for the Auger fluorescence system is  $10^{19}$  eV, and the implied RCS for the underdense case is  $\sim 2 \text{ m}^2$  at this energy. The Fresnel zone length at this range is about 250 m for a shower at 10 km altitude, corresponding to about  $10 \text{ g cm}^{-2}$  along the track. Using a commercial VHF radar system, one can easily achieve 60 kW peak power and pulse repetition rates of 10-50 kHz for 10  $\mu\text{s}$  pulses. The sky brightness temperature will lead to a system temperature of  $T_{\text{sys}} = 2000 \text{ K}$  (Kraus 1988). Using these assumptions we show the SNR budget, in dBm (decibels referenced to 1 milliwatt) in Table 1.

The implied SNR in this case is of order 800. This is not surprising, since similar radar systems are commonly used to detect comparable target areas at such ranges, at much higher frequencies. A system such as that described would be sensitive to energies down to  $10^{18}$  eV or less, and would resolve many Fresnel zones on showers of higher energy. In addition, even nearly head-on or end-on showers will likely still retain enough effective radar cross-section to produce detectable returns at  $10^{19}$  eV. The chosen chirp bandwidth of 1 MHz, given the estimated SNR, should allow range resolution of order 10 m or less. Note also that we have assumed only a single pulse here; averaging of multiple pulses will of course improve these values.

Table 1: SNR budget of a possible EAS radar system for the Auger Observatory.

Parameter	value	$\pm\text{dBm}$
<u>Received Power</u>	$\sigma_b \eta P_t G^2 \lambda^2 \times (4\pi)^{-3} R^{-4}$	
Peak transmit power	60 kW	77.8
Pulse duration	10 $\mu\text{s}$	...
chirp bandwidth	1 MHz	...
Number of repetitions	1	0.0
Antenna gain	50	34.0
wavelength	6 m	15.6
$\sigma_b$ at $E = 10^{19}$ eV	2 $\text{m}^2$	3.0
range to EAS	22.4 km	-174.0
xmit/rcv efficiency	0.1	-10.0
$(4\pi)^{-3}$	$5.04 \times 10^{-4}$	-33.0
<b>Received power</b>		<b>-86.6 dBm</b>
<u>Noise power</u>	$kT_{\text{sys}}\Delta f$	
Boltmann's constant	$1.38 \times 10^{-20} \text{ mWK}^{-1}\text{Hz}^{-1}$	-198.6
System temperature	2000 K	33.0
effective bandwidth	100 kHz	50.0
<b>Noise power</b>		<b>-115.6 dBm</b>
<b>SNR</b>	780	<b>28.9 dB</b>

The advantage of such systems for planned large area arrays such as the Pierre Auger Project is that they have the potential to greatly complement the information attained by fluorescence detectors, since they share with them the property of being able to observe showers that are distant and transverse to the observation point, and further allow for active probing of the resulting ionization rather than simple passive detection. Particle counter arrays and Cherenkov detectors must by their nature be within several hundred meters of the axis to detect the shower. Fluorescence detectors and the present proposed radar approach could be combined to produce comparable levels of information for showers that are many km from the detectors.

## 5.2. Independent ground-based radar detection of EAS

We note here that it is possible to consider an independent radar EAS detection system that does not rely on a trigger provided by another detector. Such a system could be constructed with a single transmitting station and an array of receiving stations operating in bistatic mode, arranged in a geometry that would allow post-detection triangulation of candidate events. Synchronization of stations to the ns level over tens of km baselines is routinely done using stable clocks and GPS techniques. Each individual station would store a series of candidate EAS echoes, selected by their power and short duration, and would periodically correlate the events with the other stations. System calibration could be done using meteor echoes. Such a system, operating at 30-100 MHz, could have a range of several hundred km. The system would be sensitive to radio-frequency interference, but use of chirped pulses or other more sophisticated radar pulse shapes could be used to minimize these effects.

## 5.3. Space-based EAS detection with radar

We conclude this section with a discussion of the possibility of including radar detection as a complement to the fluorescence detection on a space mission such as OWL/AirWatch. The OWL/AirWatch baseline at present is to employ an optical field of view of  $\sim 1$  sr and detect EAS fluorescence tracks with pixels giving 1 km resolution (Stalio et al. 1999). At the planned altitude in low-earth orbit of  $\sim 500$  km, the threshold energy is expected to be  $\sim 5 \times 10^{20}$  eV for a dual satellite stereoscopic version (Krizmanic et al. 1999). The necessity of stereoscopic observations has been challenged however, since it is a significant cost factor in the mission. Here we suggest that the addition of a radar system may allow for adequate information to be gathered with a single satellite.

Inspection of equation 1 shows that the radar return power varies inversely with the fourth power of the range. Thus a radar system at an altitude of 500 km (implying  $R = 560$  km to EAS near the edge of the acceptance field) will require a quite different configuration than a ground-based system.

There is a significant heritage now of space-based radar systems used for both altimetry and synthetic aperture radar (SAR) imaging (cf. Hightower et al. 1993). Most of these systems are designed for use at frequencies in the microwave range from 1-10 GHz. At these frequencies the effective RCS is inadequate, and we are forced to consider lower frequencies. At the low end, the plasma frequency of the ionosphere limits the possibilities to frequencies above about 15 MHz, and the problem of ionospheric dispersion delays further favors higher frequencies.

This dispersive delay has the magnitude  $\tau = 1.34 \times 10^{-7} \chi_e / f^2$  sec where  $\chi_e$  is the ionospheric column density in electrons  $\text{m}^{-2}$ . A typical nighttime value is  $\chi_e = 2.5 \times 10^{17} \text{ m}^{-2}$ , and the delay must be doubled for a radar signal. For  $f = 50$  MHz, the additional delay is about  $13.4 \mu\text{s}$ . The single-pass dispersion is then given by  $|\Delta\tau| = 2\tau(\Delta f/f)$  and produces an additional  $\sim 0.5 \mu\text{s}$  of pulse spread per MHz of bandwidth at 50 MHz for a roundtrip. Such dispersion may in fact be used to advantage since the dispersed return pulse has made a double pass through the atmosphere while noise of terrestrial origin is only single-pass. Thus some immunity to terrestrial impulsive noise may be achieved by using a receiver filter that is adapted to the known ionospheric dispersion.

One advantage of the long initial range to the targets of interest is that a longer chirp length may be used to improve the SNR. A reasonable compromise is a pulse length of  $\sim 50 \mu\text{s}$ , which is well-matched to many radar signal processors. This pulse length would be cleanly separated from any ground clutter for a shower at 10 km altitude. Since the roundtrip time is 3.3



ms at an altitude of 500 km, a burst of 20 pulses (at 0.15 ms intervals) is possible before the transmitter must be disabled to allow for the echo returns. This sequence could thus interrogate the ionization column  $\sim 100$  times within the first 20 ms after its formation, assuming that the fluorescence trigger can be formed within 1-2 ms. Additional pulse sequences might be used over the next 0.1-0.2 s to further improve the SNR.

Another issue of significance is the choice of antenna. At  $f = 50$  MHz ( $\lambda = 6$  m) the antenna size required to produce a beam comparable to the optical field of view is of order 6 m in diameter. However, it is desirable to suppress the side-lobe and backlobe response of such an antenna since the sky brightness temperature is much higher than that of the earth within the main beam. To do this will entail using a larger effective aperture and a ground-plane configuration that can suppress the backlobes. Also, since the fluorescence detector initially determines the direction to the shower, the antenna can be phased to interrogate this direction with a smaller main beam area and thus a higher gain.

The present OWL/AirWatch design involves a  $\sim 4$  m diameter optical reflector. Thus a ring array of deployable half-wave antennas outside of this could comprise a  $\lambda = 6$  m phased-array with a gain of  $G \simeq 50$  (half-power beamwidth of  $20^\circ$ ), steerable over the optical field of regard. Such an array could be provided with ground plane that would reduce the system temperature to  $T_{sys} \leq 1000$  K. This may or may not be possible because of constraints on the spacecraft; if not, then we expect  $T_{sys} \simeq 2000$  K due to the nonthermal galactic background emission.

Table 2 gives a summary of the tabulated SNR for a set of radar parameters that would satisfy the requirements of a mission such as OWL/AirWatch. Here we have estimated the pulse response directly using the numerical approach outlined in the appendix, for the case of normal incidence at an energy of  $3 \times 10^{20}$  eV. Using this system specified, we predict a radar SNR

Table 2: SNR budget of a space-based EAS radar system for low earth orbit.

Parameter	value	$\pm$ dBm
<hr/>		
<u>Received Power</u>	$\sigma_b \eta P_t G^2 \lambda^2 \times (4\pi)^{-3} R^{-4}$	
Peak transmit power	60 kW	77.8
Pulse duration	50 $\mu$ s	...
chirp bandwidth	5 MHz	...
Number of repetitions	100	10.0
Antenna gain	50	34.0
wavelength	6 m	15.6
$\sigma_b$ at $E = 3 \times 10^{20}$ eV	460 m <sup>2</sup>	26.6
range to EAS	560 km	-230.0
xmit/rcv efficiency	0.1	-10.0
$(4\pi)^{-3}$	$5.04 \times 10^{-4}$	-33.0
<hr/>		
<b>Received power</b>		-109.0 dBm
<hr/>		
<u>Noise power</u>	$kT_{sys}\Delta f$	
Boltmann's constant	$1.38 \times 10^{-20}$ mWK <sup>-1</sup> Hz <sup>-1</sup>	-198.6
System temperature	1500 K	31.8
effective bandwidth	20 kHz	43.0
<hr/>		
<b>Noise power</b>		-123.8 dBm
<hr/>		
<b>SNR</b>	30.8	14.9 dB
<hr/>		

of 30 for a shower at the edge of the field-of-view of the optical detectors. The compressed pulse FWHM corresponds to 200 ns in duration, and thus a range resolution of order 10-20 m should be achievable. We note that the choice of parameters described here is based on technology available off-the-shelf. In fact, integrated radar systems that meet the above requirements are available.

The significant advantage of this for an experiment such as OWL/AirWatch would be the availability of absolute ranges to the showers, as well as information about the total ion content that would complement the fluorescence data. One of the greatest sources of error in the fluorescence technique energy determination comes from the

uncertainty in the atmospheric transmission of the fluorescence emission; radar ranges would be independent of these effects. All of these together would also lead to powerful background rejection, since false triggers produced by optical flashes that might mimic EAS fluorescence would not produce radar returns. The spatial resolution for higher energy showers would also increase rapidly as the return power increased, and could thus greatly improve the information yield for cases which would otherwise be limited by the 1 km spatial resolution of the fluorescence detectors.

Of little relevance to cosmic-ray physics, but still of great interest to meteor research, is the ability of such a system to investigate high-altitude meteor ionization trails, which would appear in the same data at ranges of order 100 km less than the EAS events. This data could be acquired during the day side portion of the OWL orbit and would thus not impact the EAS investigations. OWL/AirWatch proposals (Scarsi et al 1999) have noted the possibility of optical meteor investigations; the addition of a radar system would make a much more compelling case for OWL/AirWatch as a high altitude meteor observatory.

## 6. Conclusions

We have demonstrated that, using standard models for the average behavior of extensive air shower development, the resulting ionization is straightforward to detect using radar techniques in the VHF frequency range (30–100 MHz), for primary energies greater than about  $10^{18}$  eV. We estimate that a relatively modest ground-based system, utilizing a trigger from an existing air shower array such as the Fly’s Eye HiRes system in Utah, could estimate ranges to these showers with a precision of order 20 m. More sophisticated systems may be able to provide detailed information on shower structure for arrays such as the Auger Observatory, and possibly even work as standalone detectors for such showers.

We have also analyzed the potential for using such a system on a space mission such as OWL/AirWatch, and we find that a VHF radar system appears capable of detecting and ranging showers of energies above  $\sim 10^{20}$  eV with a precision of  $\sim 20$  m, and a spatial resolution at least as good as the planned optical imaging system, and which improves significantly for higher energies as the echo return power grows.

We thank David Saltzberg and George Resch for useful discussion and comments. This research has been performed at the Jet Propulsion Laboratory, California Institute of Technology, under contract with the National Aeronautics and Space Administration.

## REFERENCES

- Balanis, C. A., 1997, *Antenna Theory*, 2nd edition, (New York: Wiley & Sons).
- Baltrusaitis, R. M., Cady, R., Cassiday, G. L., Cooper, R., Elbert, J. W., Gerhardy, P. R., Ko, S., Loh, E. C., Salamon, M., Steck, D., & Sokolsky, P., 1985, NIM A240, 410.
- Bourdeau, M. F., et al., 1980, J Phys. G: Nucl. Phys. 6, 901.
- Buonsanto, M., Sipler, D. P., Davenport, G. B., & Holt, J. M., 1997, J. Geophys. Res. 102 (17), 267.
- Capelle, K.S., Cronin, J.W., Parente, G., & Zas, E., 1998, Astropart. Phys. 8, 321.
- Dawson, B.R. et al., 1997, Proc. 25th International Cosmic Ray Conf., Durban, OG 10.6.16.
- Greenhow, J. S., 1952, Proc. Phys. Soc. B, 65, 169.
- Greisen, K., 1965, in Prog. Cosmic Ray Physics vol. III, J.G. Wilson ed., (North Holland: Amsterdam) 1.
- Guérard, C. K., et al. 1998, Proc. Workshop Front. Astroph. & Part. Physics, Vulcano, Sicily.

Hanbury Brown, R., & Lovell, A. C. B., 1962, *The Exploration of Space by Radio*, 2nd ed., (New York: Wiley).

Hightower, C. H., Brown, T., & Soon, N. Y., 1993, Proc. of the IEEE Nat. Radar Conf., 6.

Jones, J. & Jones, W. 1991, Planet. Space Sci. 19(9), 1289.

Jones, W., 1991, Planet. Space Sci. 1991, 19(9), 1283.

Kaiser, T. R., & Closs, T., 1952, Phil. Mag. 43, 1.

Kamata, K., & Nishimura, J., 1958, Suppl. Progr. Theoret. Phys. 6, 93.

Kraus, J. D., 1988, *Antennas*, 2nd ed., (New York: McGraw-Hill).

Krizmanic, J. et al., 1999, Proc. 26th Int. Cosmic Ray Conf., eds. Kieda, Dingus & Salamon, (Univ. Utah: Salt Lake City) vol 2, 388.

Lovell, A.C.B., & Clegg, J. A., 1948, Proc. Phys. Soc. 60, 491.

Poulter, E. M., & Baggaley, W. J., 1977, Journ. Atmos. Terrest. Phys. 39, 757.

Rosner, J. L., and Wilkerson, J. F., 1997, appendix to the proposal for the Auger Air Shower Array; hep-ex/9702008.

Scarsi, L. et al., 1999, Proc. 26th Int. Cosmic Ray Conf., eds. Kieda, Dingus & Salamon, (Univ. Utah: Salt Lake City) vol 2, 384.

Seaton, M., 1959, MNRAS 119, 81.

Segre, E., 1977, *Nuclei and Particles*, 2nd ed., (Reading, MA: Benjamin/Cummings).

Skolnik, M., 1990, *Radar Handbook*, (New York: McGraw-Hill), 2nd ed.

Stalio, R. et al. 1999, Proc. 26th Int. Cosmic Ray Conf., eds. Kieda, Dingus & Salamon, (Univ. Utah: Salt Lake City) vol 2, 403.

Thomas, L. 1972, Journ. Atmos. Terr. Phys. 33, 157.

Wehner, D. R., 1987, *High Resolution Radar*, (Norwood, MA: Artech House).

## A. Appendix: Numerical Evaluation of RCS for the underdense case

To estimate the RCS for the underdense regime of an EAS ionization column, we need to evaluate the individual contributions of the scattering electrons and the phase of the resulting scattered fields. As noted in section 2 above, under certain conditions this is equivalent to determining the Fourier transform of the electron distribution. Here we describe the basis for this conclusion and provide details of the methods used for numerical evaluation of the RCS under these circumstances.

### A.1. Geometry of the problem

The geometry for this evaluation is shown in Fig. A8. Here we let  $\mathbf{R}$  represent the vector distance from the origin  $O$  (at the radar transmitter/receiver) to the position of shower maximum. We choose the  $x - y$  plane to be coincident with the plane containing the axis of the shower and  $\mathbf{R}$ . Within the ionization column itself, we use cylindrical coordinates  $\rho, \phi, z_1$  to calculate the proper ionization density at position  $P$  with respect to the position of shower maximum;  $\mathbf{r}' = (\rho, \phi, z_1)$  is the vector separation of  $P$  from shower maximum. The vector joining the origin to  $P$  is denoted as  $\mathbf{r}$ . The angle between the shower axis and  $\mathbf{R}$  is denoted  $\theta$ .

Given these definitions, we find

$$|\mathbf{r}|^2 = \rho^2 + z_1^2 + R^2 + 2R(\rho \cos \phi \sin \theta - z_1 \cos \theta) \quad (\text{A1})$$

which expresses the distance to an arbitrary point in the ionization column as a function of the distance to shower maximum, the local cylindrical coordinates of the point, and the angle of

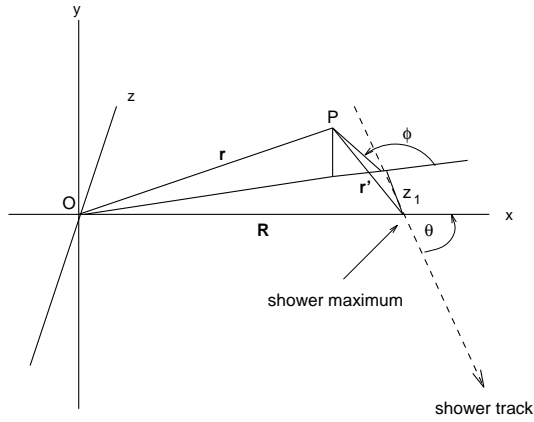


Fig. A8.— The geometry for numerical evaluation of the summed radar cross section of an ionization column for the case of oblique angle of incidence. The radar transmitter/receiver is at the origin  $O$ , and the angle of the track is  $\theta$  with respect to the direction from the origin to shower maximum  $R$ . The vector to the position  $P$  in the ionization column that is being evaluated is  $\mathbf{r}$ , and the vector separation of  $P$  from the position of shower maximum is  $\mathbf{r}'$ .  $\phi$  is the azimuthal angle of  $P$  in cylindrical coordinates with respect to the shower axis.

obliquity  $\theta$  of the shower.

## A.2. Scattered field

The electric field that is incident at  $P$  can be written as

$$U_{inc} = U_{tr} G_{tr} e^{i\omega t} \frac{e^{i\mathbf{k}\cdot\mathbf{r}}}{|\mathbf{r}|} \quad (\text{A2})$$

where  $U_{tr}$  is the magnitude of the transmitted field,  $G_{tr}$  is the transmitter gain factor (as defined in the main text),  $k = 2\pi/\lambda$ , and  $\mathbf{r}$  is defined in Fig. A8. Assuming that  $\mathbf{k}$  and  $\mathbf{r}$  are parallel (that is, neglecting the effective dielectric behavior of the underdense plasma in the column), the received field from a small volume of electrons  $n_e dV$  which scatter coherently is then given by

$$dU_{rcv} = U_{inc} \sqrt{\sigma_T} n_e dV G_{sc} e^{i\omega t} \frac{e^{i\mathbf{k}_{sc}\cdot\mathbf{r}_{sc}}}{|\mathbf{r}_{sc}|} \quad (\text{A3})$$

where  $G_{sc}$  is the effective gain of the electron scattering process ( $G_{sc} = 1$  for isotropic scattering),<sup>3</sup> and  $\mathbf{k}_{sc}$ ,  $\mathbf{r}_{sc}$  are the wavevector and radial vector of the scattered wave. In this case we have  $\mathbf{k}_{sc} = -\mathbf{k}$  and  $\mathbf{r}_{sc} = -\mathbf{r}$ , and thus

$$dU_{rcv} = U_{tr} G_{tr} G_{sc} \sqrt{\sigma_T} n_e dV e^{i\omega t} \frac{e^{2i\mathbf{k}\cdot\mathbf{r}}}{|\mathbf{r}|^2} \quad (\text{A4})$$

which displays the expected radial dependence of the field (equivalent to a  $r^{-4}$  dependence in received power), and also the additional factor of two in the spatial phase which is due to the two-way trip of the radiation.

If we assume for the moment that the time variation of the field is steady-state, we can drop the time dependence, and integrate over the volume of the shower to yield the total received field strength, assuming that the transmitted beam is larger than the dimensions of the shower. If we

<sup>3</sup>For Thomson scattering,  $G_{sc} \simeq 1.6$  corresponding to electric dipole emission. However, this response is complicated in any real plasma by a number of effects, and we have assumed  $G_{sc} = 1$  for all cases considered here.

also assume that the distance from the shower is large enough that  $|bfr| \approx |\mathbf{R}|$ , then we have

$$R^2 U_{rcv} = U_{tr} G_{tr} G_{sc} \sqrt{\sigma_T} \int_V n_e(\mathbf{r}) e^{i\mathbf{q} \cdot \mathbf{r}} d^3\mathbf{r} \quad (\text{A5})$$

which shows (taking  $\mathbf{q} = 2\mathbf{k}$ ) that the received field is proportional to the Fourier transform of the electron density distribution.

### A.3. Normal incidence

Under conditions where the pulse is incident on the ionization column at normal incidence, and if we assume that the ionization column is essentially constant along its longitudinal length, the received field becomes proportional to the two-dimensional Fourier transform of the cross-sectional electron density, times the length of the Fresnel zone  $L_F$  (defined as the length over which the scattered fields are in phase):

$$R^2 U_{rcv}|_{\theta=0} = U_{tr} L_F G_{tr} G_{sc} \sqrt{\sigma_T} \int_A n_e(\mathbf{r}) e^{i\mathbf{q} \cdot \mathbf{r}} d^2\mathbf{r}. \quad (\text{A6})$$

We have numerically evaluated this using Fast Fourier transform techniques, since the area  $A$  over which this is done is of order  $A = \pi r_m^2$  and the number of  $\lambda_{min}/8$  cells in the grid is  $64A/\lambda_{min}^2$ , where we have assumed  $\lambda_{min} \sim .5$  m, giving a  $(2^{13})^2$  grid. The result of the FFT can be normalized to provide a frequency-dependent phase factor, which we have plotted in Fig. 4.1 above.

### A.4. Pulsed radar & the time-projected RCS

In the previous analysis we have assumed a steady-state radar (also known as carrier-wave or CW radar). However, in our analysis of section 4, we assumed that the radar is pulsed, and in fact pulsed radar is necessary to achieve the kind of time resolution required in this application. For the overdense case, the analysis presented in section 4 is adequate, since we are considering reflections from a localized source at the

critical radius of the ionization column. Also, for normal incidence, the reflections from the first Fresnel zone arrive closely in phase and can be treated without explicitly accounting for the pulse echo behavior.

When we allow for oblique shower angles, however, the concept of the Fresnel zone loses its usefulness, and the received echo comes from the entire volume of the shower and is thus significantly spread out in time. We require a method of treating the behavior of a discrete pulse under these conditions.

The approach we have followed is intuitively simple: we first produce a time profile of the time-projected electron density; that is, we calculate the time associated with the global phase of each of the contributing differential volume elements of the scattering electrons

$$t_i = \frac{\lambda}{2\pi c} \mathbf{q} \cdot \mathbf{r}_i. \quad (\text{A7})$$

Here  $t_i$  is the round-trip time for the  $i$ th volume element at location  $\mathbf{r}_i$ . If we consider all of the volume elements for which  $t_i = t_j$  within a specified interval  $\Delta t \leq \omega^{-1}$ , then we define a shell at distance  $r = t/2c$  with a thickness of 1 radian of phase at the radar angular frequency  $\omega$ .

Summing all of the contributing elements in this shell gives the time-projected square root of the total cross section at that phase:

$$Y(t)\Delta t = \sqrt{\sigma_T} \int_{r-t/4c}^{r+t/4c} n_e(\mathbf{r}) d^3\mathbf{r}. \quad (\text{A8})$$

Once  $Y(t)$  is determined for a given radar wavelength, shower angle and energy, and distance, then the pulse response of the ionization column is determined by convolving the electric field of the pulse profile with  $Y(t)$ , and squaring the result. If the pulse is defined to have unit amplitude, then the resulting convolution can be expressed as an effective radar cross section for use in equation 1.

For example, if the pulse is assumed to be a  $\delta$ -function in time, the resulting convolution  $\Upsilon(t)$

is

$$\Upsilon(t) = \int_{-\infty}^{\infty} Y(t')\delta(t-t')dt' = Y(t) \quad (\text{A9})$$

and the received power is then proportional to  $|Y(t)|^2$ . For other pulse profiles we numerically evaluate the convolution explicitly, and take the maximum of the resulting profile to be the effective radar cross section.

In Fig. A9 we show an example of the square of  $Y(t)$ , giving the time-projected cross section calculated according to the manner described here. In each case the time bins correspond to a radian of angular phase according to the wavelength indicated, and the value for each bin is estimated according to equation A8. The profile in this case shows a characteristic rapid rise on its leading edge, reflecting the rise in cross-sectional ionization density of the nearest portion of the shower. The more slowly falling trailing edge is due to the contributions from portions of the shower further away.

We note that  $Y(t)$  defined in this way is analogous to a Green's function for the time response of the system. It can be used in this manner to evaluate arbitrary radar pulse shapes, for a given EAS energy and direction. For extremely broad-band radar systems, the effective RCS values will begin to approach those of  $Y(t)$ . For more narrow-band radar pulses, the convolution of the field oscillations with  $Y(t)$  will act to partially cancel and the effective RCS will decrease.

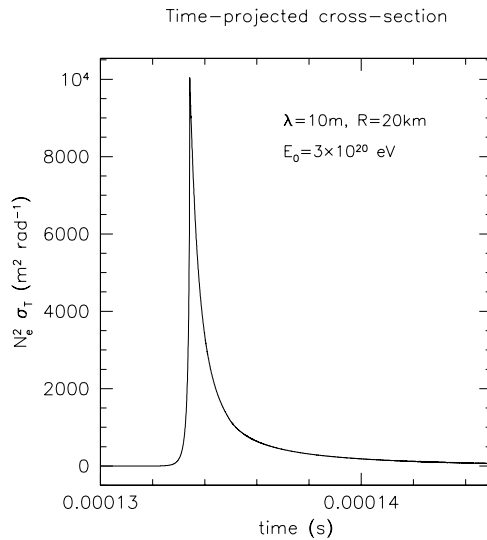


Fig. A9.— The square of the function  $Y(t)$ , which gives the time-projected total radar cross section, for an ionization column produced by a shower with  $E_0 = 3 \times 10^{20}$  eV, for  $\lambda = 10$  m, at a distance of 20 km. The time axis is windowed around the arrival time of the round trip travel time.  $Y(t)$  may be thought of as a kind of Green's function time response of the ionization column to a sharp radar pulse, with a magnitude that is proportional to the square root of the RCS at a given pulse phase.